The Effects of Inhomogeneities and Anisotropies on Electrocardiographic Fields: A Three-Dimensional Finite Element Study

Ruth Nicholson Klepfer, Christopher R. Johnson, and Robert S. Macleod
Department of Bioengineering, Department of Computer Science,
and the Cardiovascular Research and Training Institute
University of Utah, Salt Lake City, UT 84112.
E-Mail: `rklepfer@cs.utah.edu`, `crj@cs.utah.edu`, `macleod@cvrti.utah.edu`
Web: http://www.cs.utah.edu/~sci/

March 10, 1997

Contents

Abstract

The aim of this study was to quantify the effects of selected inhomogeneities and anisotropies on computed electric potential fields associated with the electrocardiographic forward problem. The model construction was based on the Utah Torso model and included geometry for major anatomical structures such as subcutaneous fat, skeletal muscle, and lungs, as well as for epicardial fatpads, major arteries and veins, and the sternum, ribs, spine and clavicles. Measured epicardial potentials served as the electrical source for solutions to the electrocardiographic forward problem computed using the finite element (FE) method. The geometry of the torso model for each simulation was constant but different combinations of conductivities were assigned to individual organs or tissues. Comparisons of different conductivity combinations followed one of two basic schemes: 1) a homogeneous torso served as the reference against which we compared simulations with a single organ or tissue assigned its nominal conductivity and 2) a fully inhomogeneous torso served as the reference and we removed the effect of individual organs or tissues by assigning it the homogeneous conductivity value. When single inhomogeneities were added to an otherwise homogeneous isotropic model, anisotropic skeletal muscle (at a 15:1 anisotropy ratio) and the right and left lung had larger average effects (12.8, 12.7 and 12.1 percent relative error, respectively) than the other inhomogeneities tested. Our results for removing single inhomogeneities show that the subcutaneous fat, the anisotropic skeletal muscle (with the degree of anisotropy equal to 7:1), and the lungs have larger average impacts on the body surface potential distributions than other elements of the model (with values of 14.9, 12.6 and 11.7 percent relative error, respectively). The results also show that the size of the effect depended strongly on the distribution of epicardial potentials. The results of this study suggest that accurate representation of tissue inhomogeneity has a significant effect on the accuracy of the forward solution, with regions near the torso surface playing a larger role, in general, than those near the heart.

Keywords

Anisotropy, electrocardiography, finite element method, forward problem, inhomogeneity.

I. Introduction

Computer models of electric fields in the human torso have numerous applications and are useful as a substitute for invasive measurements [1], [2], [3]. A few examples of modeling applications include electrical impedance tomography [4], the study of bioelectric fields from the heart [5], [6], and design and optimization of implantable defibrillators [7]. As the cost of high-speed processing and computer memory has decreased, it has become increasingly practical to model larger and more realistic problems. In each modeling scenario encountered, however, the details of the physiology are still too numerous and too complicated to be fully modeled, even with the most powerful computational systems currently available. In the specific case of the electric fields arising in the thorax due to the heart, the level of detail of the two most important aspects of the simulation—the geometrical model of the thorax and the conductivity values assigned to each region of the geometry—is still very limited. The simplest assumption is that conductivity is homogeneous (the same material properties apply throughout the volume) and isotropic (material properties do not depend on the orientation of field vectors). More detailed models attempt to characterize tissue inhomogeneity and anisotropy by including one or more inhomogeneous regions. However, while the role and relative importance of inhomogeneities for specific electrocardiographic situations has been the topic of many different thorax model studies [8], [9], [10], [11], [12], [13], [14], [15]; there is currently no consensus on the subject among researchers. The goal of the study reported here was to evaluate, through the use of advanced numerical techniques and a detailed model of the human torso, the role of inhomogeneities (including anisotropic ones) in computing forward solutions from epicardial heart potentials.

Several specific aspects of electric fields in the thorax further complicate the inclusion of inhomogeneities in model geometries. The first is the fact that torso conductivities cover a wide range: the electrical conductivity of blood, for example, is over 47 times larger than that of bone [16]. In addition, the inhomogeneity of the electric field within the thorax, together with the asymmetry of its geometric structures, suggest that not only the values but also the locations of conductive inhomogeneities will influence field calculations. Finally, the field distribution within the thorax during a heart beat is dynamic in nature. While the frequencies that arise are considered low enough to treat the problem as quasi-static in nature [17], the interaction between electric field and resistive tissues will vary in time due purely to spatial variation in the field. Hence, there exists a need to consider the influence of a wide variety of tissues on model calculations and to evaluate them under a dynamic range of conditions.

In this study, we evaluated the effects of selected inhomogeneities and anisotropies on computed body surface potential maps (BSPMs) in a large-scale model of the human thorax. The results can serve to guide the selection of inhomogeneities to include in any geometric model used to compute bioelectric fields. It should be noted that it is currently not possible to measure epicardial and body surface potential distributions simultaneously in humans and thus data for absolute validation are not available. What these results can establish, however, is the relative effect of selectively including or excluding a wide variety of inhomogeneities in a detailed model of the human thorax.

II. Methods

A. Problem Formulation

The bioelectric fields produced in the human thorax can be mathematically described by Maxwell's equations. For electrostatic problems in dielectric volume conductors, an electric field, $\mathbf{E}$, can be described in terms of the gradient of a scalar potential field Φ [18]

$$\mathbf{E} = -\nabla\Phi. \tag{1}$$

In the frequency range of the electrocardiographic signals (0–100 Hz [19]), the volume conductor can be considered purely resistive so that a quasi-static approximation is justified [20].

Thus the current density associated with the electric field is given by Ohm's law,

$$\mathbf{J} = \sigma \mathbf{E}, \tag{2}$$

where $\mathbf{J}$ is the current density and σ is the electrical conductivity of the tissue, represented mathematically as a 3×3 symmetric tensor. If active current sources are also present, this equation becomes

$$\mathbf{J} = \sigma \mathbf{E} + \mathbf{J_i}. \tag{3}$$

Under quasi-static conditions, the net current flow is solenoidal such that the divergence of equation (3) is zero. Therefore,

$$\nabla \cdot \mathbf{J} = \mathbf{0} = \nabla \cdot \sigma \mathbf{E} + \nabla \cdot \mathbf{J_i} \tag{4}$$

$$-\nabla \cdot \mathbf{J_i} = \nabla \cdot \sigma \mathbf{E}. \tag{5}$$

Substituting equation (1) into equation (5), we obtain

$$\nabla \cdot \mathbf{J_i} = \nabla \cdot \sigma(\nabla \Phi) \tag{6}$$

or

$$\nabla \cdot (\sigma \nabla \Phi) = -I_{sv} \text{ in } \Omega, \tag{7}$$

where

$I_{sv} =$ internal current source per unit volume, and
$\Omega =$ bounded volume domain,

which is a form of Poisson's equation.

For this study, $I_{sv} = 0$, because we bound the volume of interest by the epicardial and body surfaces so that all sources are outside the bounded volume domain. As such, equation (7) simplifies to a general form of Laplace's equation. By applying the Dirichlet and Neumann boundary conditions, we can formulate an electrocardiographic forward problem in terms of epicardial sources as

$$\nabla \cdot (\sigma \nabla \Phi) = 0 \text{ in } \Omega, \tag{8}$$

with

$$\Phi = \Phi_0 \text{ on } \Gamma_E \tag{9}$$

$$(\sigma \nabla \Phi) \cdot \mathbf{n} = 0 \text{ on } \Gamma_T, \tag{10}$$

where

$\Phi_0 =$ electric potential on the epicardial surface boundary (known *a priori*),
$\Gamma_E =$ boundary at the epicardial surface, and
$\Gamma_T =$ boundary at the torso surface [21].

B. Numerical Methods

To solve equation (7) numerically, we first applied a Galerkin formulation and then utilized the finite element method with linear basis functions and tetrahedral volume elements. The finite element method has three strengths over other methods for this type of computation. First, it allows explicit modeling of the anisotropic conductivities of skeletal muscle. The finite element method computes an estimate of the potential field over each element, taking into account the material properties of each individual element. Therefore, it is possible to specify different conductivity tensors over different regions, or even for each element. Secondly, the finite element method supports unstructured meshes. This permits us to use an adaptive, unstructured mesh density that can model complicated geometries while simultaneously minimizing numerical discretization error. Finally, as long as tissue regions are identified and boundaries are maintained, the finite element method allows very flexible assignment of tissue characteristics. For example, altering the conductivity of the lungs required changing only a single entry in a look-up table that linked tissue types with conductivity values.

Applying the finite element method to equation (7) results in a system of linear equations, $A\Phi = b$, where the matrix A contains the geometry and conductivity information for the problem and has the properties of being sparse, symmetric, and positive definite. The solution of this system provides the potential at each node in the discretized model geometry. Because the matrix A is symmetric and positive definite, a Choleski preconditioner can be used to accelerate the rate of convergence of iterative solvers. We utilized a preconditioned Incomplete Choleski Conjugate Gradient (ICCG) method to iteratively solve the linear system.

C. Geometry Discretization

The model in this study was constructed primarily from 115 transverse MRIs of a healthy adult male. The images were taken every 5 mm beginning just below the waist and ending at the bottom of the neck. In each two-dimensional image, the regions of interest were segmented into contours. Figure 1 shows the segmentation contours of several major regions in one of the images that included the heart. The segmentation was accomplished with a segmentation program that allowed the user to view the MRI to manually select boundary points with a mouse [22], [23]. The points for each contour were used to create a spline that was then resampled to establish regular spacing and saved as a set of x, y coordinates describing the contour at a particular z level. In this way, regions of particular tissue types (for example, subcutaneous fat) as well as anatomical structures (such as the right atrium) were specified. The larger tissue regions of the model included the subcutaneous fat, the skeletal muscle, the lungs and the bones of the torso. In the vicinity of the heart, more detailed anatomical structures were specified. These structures included both atria and ventricles, three epicardial fat pads and the following components of the great vessels: the superior and inferior vena cava, the pulmonary arteries and veins, the ascending and descending aorta, the azygous vein, and the left and right subclavian veins. All of the contours in the different z planes for a particular structure, such as a lung, were then connected into triangles to construct a closed surface.

For each closed surface, a Delaunay optimal tetrahedral mesh was then generated to discretize the volume of the thorax (the mesh generator used for this study is described in detail elsewhere [24], [25]). Tetrahedra were chosen because of their ability to approximate the irregular surfaces and volumes of the human body and because they are well suited to fully automatic mesh generation algorithms. As part of the tetrahedralization procedure, each element also received a group number based on the tissue type assigned to the cell. This group number later served as the means of flexibly assigning conductivity values to each element in the model. Figure 2 shows a cutaway of the outer torso surface with the triangulated surfaces of the lungs and the epicardium inside.

In a second iteration of constructing the Utah Torso, we incorporated the following bones into the torso model: the left and right clavicle, the sternum, all 12 left and right ribs, and the spinal column. Because the bones were not well defined in the MRIs, surface geometry for these structures was

Fig. 1. Magnetic resonance image of the thorax with superposed segmentation boundaries. The projection of the image is caudal-cranial and tissue boundaries include subcutaneous fat, lungs, and epicardial and endocardial borders of the heart.

obtained from Viewpoint (Orem, Utah), a commercial supplier of three-dimensional geometry data sets. The point coordinates were scaled and shifted to fit within the Utah Torso. The mesh of the bones was then generated with the same code used for the structures obtained from the MRIs. The complete torso mesh had approximately one million tetrahedra and 168,000 nodes. The simulations in this study were all calculated using a single mesh. If different meshes were used based on the different inhomogeneities being modeled in a particular scenario, the effects calculated would be even greater.

D. Material Properties

Electric conductivity is the material property of interest in modeling electrocardiographic fields. At a microscopic level, the discrete nature of cell structure dictates that all tissue is anisotropic; however, at a macroscopic level, many tissues can be approximated as having isotropic conductivity in the 0–100 Hz bandwidth that is considered relevant for electrocardiography [17]. The exception is the skeletal muscle, which maintains anisotropic properties even at a macroscopic level. We implemented anisotropy in this model by specifying a 3×3 conductivity tensor with different values for each direction of conductivity. Each tetrahedra was automatically assigned a conductivity tensor according to the tissue type to which it belonged. All tissues, except skeletal muscle, were modeled as isotropic and piecewise homogeneous. In the isotropic case, the conductivity tensor reduces to a scalar, while for anisotropic regions it is a 3×3 symmetric tensor.

The conductivity values used for the tissue types in this model were taken from the comprehensive review article of Foster and Schwann [16]. Conductivity in living tissue varies sharply with frequency and Figure 3 demonstrates the large range of conductivity values found among the tissues in the torso for the 0–100 Hz range. The homogeneous torso conductivity, .239 S/m, is the mean of the conductivities of the other tissues and was used for the homogeneous torso model.

Within the skeletal muscle that surrounds the thorax, fiber orientation—and hence conductivity—changes constantly. To approximate the resulting directional conductivity, we considered the torso to be a cylinder around which the muscle fibers wrap. We then split the torso into twelve 30 degree sections or slices and assumed the fiber direction of each slice to be perpendicular to the bisector of the slice. Figure 4 shows a schematic of the fiber directions. Anisotropy ratios indicate the relative conductivities along (logitudinal) and perpendicular to (radial) the local fiber direction. Longitudinal to radial conductivity ratios in the simulations ranged from 1:1 (isotropic) through 3:1, 5:1, 7:1 (the value cited in most literature [16]), 10:1 to 15:1.

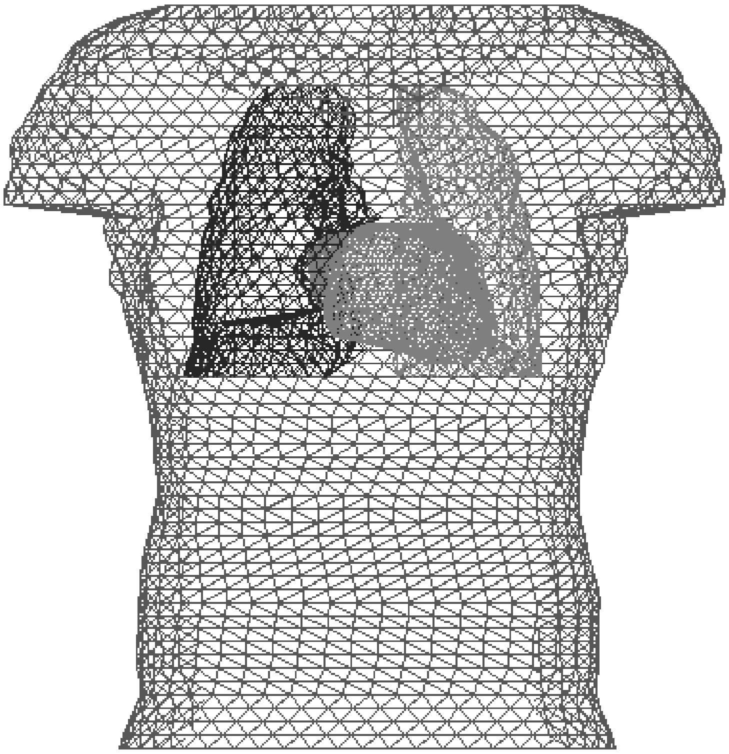

Fig. 2. Frontal view of the surface triangulation of the Utah torso model. Surfaces included in the figure are torso boundary, lungs, and epicardium. Internodal spacing ranged from 5–10 mm.

E. Boundary Condition Data

The boundary conditions for the solution to equation (9) require that the electric potentials at all nodes of the epicardium be known *a priori*. The epicardial potentials for these simulations were recorded from a patient during the surgical ablation of an accessory pathway to treat Wolff-Parkinson-White syndrome. An electrode sock containing 64 silver wire electrodes was placed over the ventricles during open chest surgery [26], [27], and all 64 channels were sampled every millisecond across several heartbeats. Applying equations 8 and 9 to the geometrical model requires a surface that encloses all the cardiac sources. The measured data that make up the boundary conditions, however, are limited to the outer surface of the ventricles. For these simulations, we created a boundary surface that included the ventricular epicardium and a pseudo-surface "cap" corresponding approximately to the base of the heart between ventricles and atria. The atria then fell outside the source region and were treated as passive, blood-filled compartments. In order to generate potentials for all 1112 epicardial surface nodes from the 64 recording sites, we performed surface interpolation. First, each measurement site was mapped to a node in the geometrical model; then, Laplacian interpolation was performed [28], [29]. For the purpose of these simulations, we selected 30 time instants, spaced at 2 millisecond intervals and covering the entire QRS complex. The QRS represents the ventricular activation phase of the heart cycle, and, thus, is the most rapidly changing portion of the ECG; potential distributions also exhibit the largest spatial gradients during this period. By focusing on this part of the signal, we hoped to apply a variety of boundary conditions and thus reveal a wide range of effects of inhomogeneities.

III. Simulations

To address the goal of our simulation study, we carried out two types of simulations. First, we wished to determine the effect of selectively adding inhomogeneous regions to an otherwise homogeneous

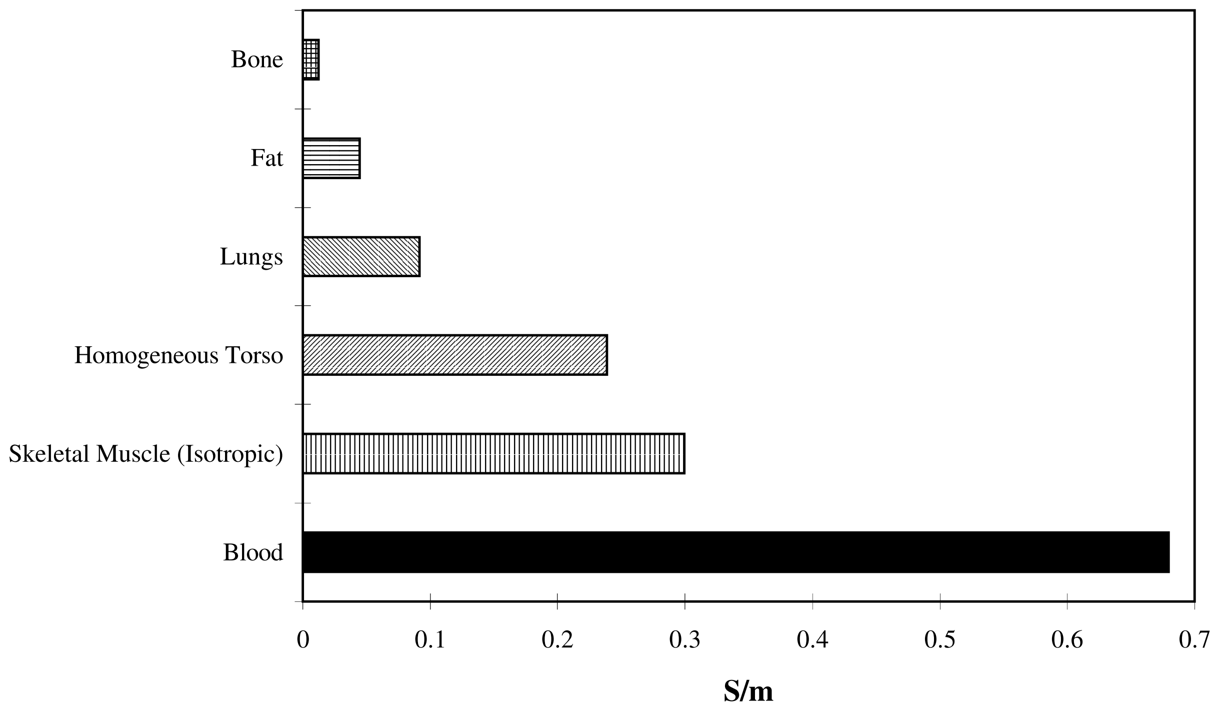

Fig. 3. Range of conductivies assigned to different regions of the torso model.

model. To this end, we computed potentials for each of the same 30 time instants, first with a completely homogeneous model and again after including a single inhomogeneity. Then we compared the solutions statistically with the homogeneous solution as the reference. The inhomogeneities studied did not necessarily belong to a single closed region. For example, all of the bones were tested as a single inhomogeneity. Some larger structures, such as the lungs, were considered both individually and in combination in order to evaluate the effect of similar structures in different proximities to the heart. We considered the following individual inhomogeneities: the bones, the left lung, the right lung, both lungs, subcutaneous fat, isotropic skeletal muscle, anisotropic skeletal muscle at 5 different anisotropy ratios (3:1, 5:1, 7:1, 10:1 and 15:1), the major blood vessels in the vicinity of the heart, and three epicardial fatpads, two located in the atrioventricular groove and the other one on the apex of the heart. "Including" an inhomogeneity actually meant assigning an appropriate conductivity value to all elements with a group number corresponding to that inhomogenetity. The rest of the tetrahedra were assigned the average isotropic conductivity, listed in Figure 3 as homogeneous torso, of .239 S/m.

The second type of simulation was a complement of the first – its goal was to evaluate the effect of *removing* a single inhomogeneity from an otherwise completely inhomogeneous model. In this case, the reference model, or full model, included all available inhomogeneities. The skeletal muscle in this model was assigned a 7:1 anisotropy ratio. Simulations were then run at the same time steps but with a specific region assigned the average isotropic conductivity tensor. The potentials from these simulations were compared to those from the reference model. The list of inhomogeneities removed from the full model was similar to that from the first study: subcutaneous fat, 7:1 skeletal muscle, both lungs, the bones, the major blood vessels, all the fatpads, and each individual fatpad.

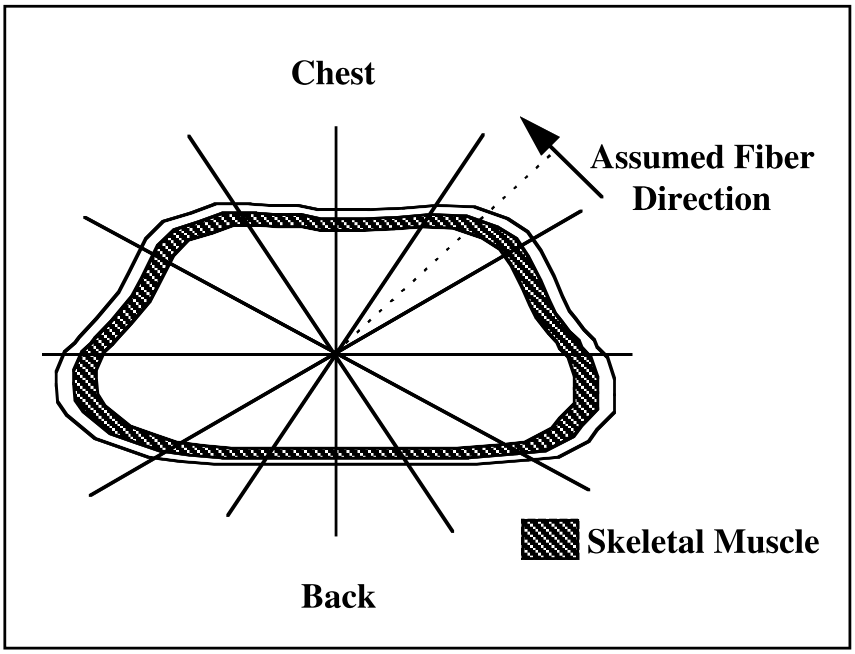

Fig. 4. Anisotropic conduction assignment for the skeletal muscle. Fiber direction of the muscle was assumed to be perpendicular to the bisector (shown as dashed line) of each of 12 sectors (shown bounded by solid lines) in the torso cross section.

A. Analysis

Simulation results were evaluated by comparing only the nodes on the torso surface, the computed equivalent of a body surface potential map (BSPM). Figure 5 shows examples of BSPMs for two different simulations and their difference at three different time instants. The examples in the top row were calculated using a completely homogeneous model; the examples in the middle row were calculated using the full model. The examples in the third row were calculated by taking the difference between the homogeneous and the full map at that time instant. The number above the upper left corner of each map is the time instant the map represents, which are also marked as vertical lines on the time signal in the upper right-hand corner. The maps are two-dimensional projections of the torso with the anterior of the torso on the left half and the posterior on the right half. Each map has the positive and negative peaks marked on the map with a plus or minus sign and labelled. The dashed contours represent negative values and the solid lines represent positive values.

The fluctuation of the difference maps with time indicates that the effects of inhomogeneities vary with field distribution and should be studied under conditions of realistic epicardial potentials as functions of time. As described in Section II-E, we generated results for each instant in time through the entire QRS of a single beat recorded from a patient. In order to capture the temporal variation, we report statistical differences both as functions of time as well as averaged over the entire beat.

The statistical parameters used to compare maps were the root mean squared error (E_{RMS}), the relative error (RE), and the correlation coefficient (CC), computed as follows:

$$E_{RMS} = \sqrt{\frac{\sum_{i=1}^{N}(\Phi_i^{calc} - \Phi_i^{ref})^2}{N}} \tag{11}$$

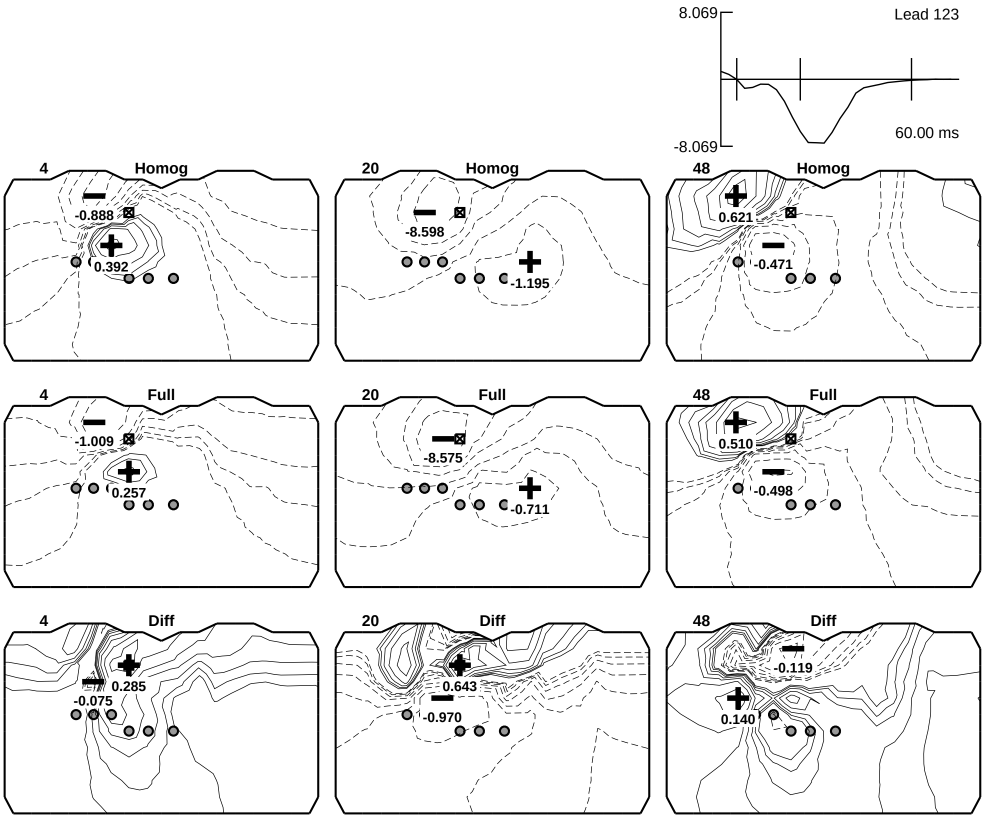

Fig. 5. Computed BSPMs under different conductivity assumptions. Each map is a projection of the torso surface with the anterior region in the left half of each map and the (shared) edges corresponding to the right mid-axillary line. Contours indicate isopotentials spaced logarithmically and scaled individually for each map; solid lines indicate positive potentials and dashed lines negative potentials. The extrema for each map are marked and labeled. In the time signal trace in the upper, rightmost panel, the three vertical lines indicate the time instants selected for maps displayed in each column of the figure. The rows of maps differ in the conductivities assumed with the homogenous torso used to generate the results shown in the uppermost row, the full inhomogeneous torso in the middle row and their difference displayed in the lowest row.

$$RE = \sqrt{\frac{\sum_{i=1}^{N}(\Phi_i^{calc} - \Phi_i^{ref})^2}{\sum_{i=1}^{N}(\Phi_i^{ref})^2}} \tag{12}$$

$$CC = \frac{\mathbf{\Phi^{calc}} \cdot \mathbf{\Phi^{ref}}}{\mid \mathbf{\Phi^{calc}} \mid\mid \mathbf{\Phi^{ref}} \mid}. \tag{13}$$

The reference values, Φ^{ref}, are either the potentials computed with the homogeneous model in the first set of simulations or the potentials from the full model for the second set of simulations.

IV. Results

While all three measures, E_{RMS}, RE, and CC, were calculated for each pair of maps, the values for E_{RMS} and RE responded identically to changes in inhomogeneities. Hence, we include only plots of RE and CC. The calculated E_{RMS}, RE and CC values for all the simulations can be found on the World Wide Web at http://www.cs.utah.edu/~rklepfer/inhomogstudy.html. Note that the actual values of RE depend on the value chosen for the homogeneous isotropic conductivity.

Figures 6 and 7 show the RE for simulations in which a single inhomogeneity was added to the otherwise homogeneous isotropic torso. The data has been split into two figures to improve readability.

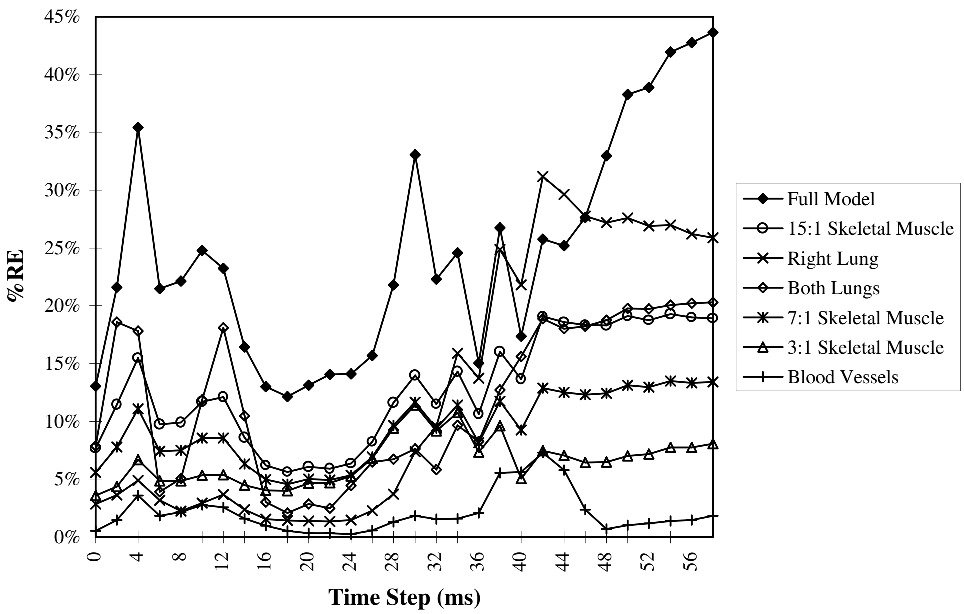

Fig. 6. Values of RE between BSPMs computed with the homogeneous torso and those computed using the torso with the addition of the listed inhomogeneity as a function of time through the 60 ms of the QRS of a single beat.

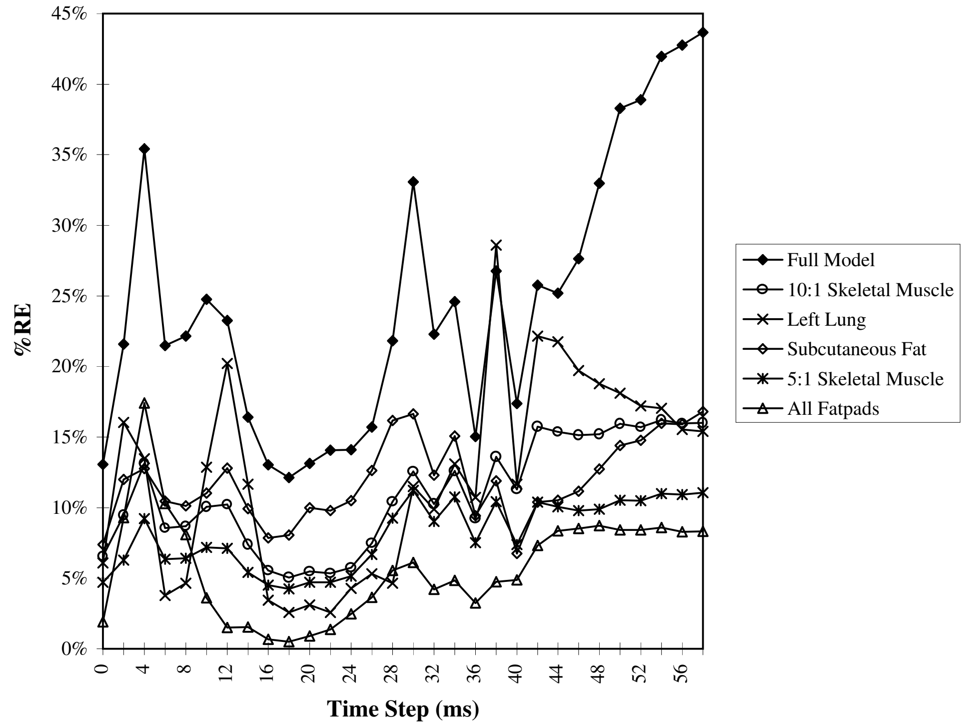

Fig. 7. Values of RE between BSPMs computed with the homogeneous torso and those computed using the torso with the addition of the listed inhomogeneity as a function of time through the QRS.

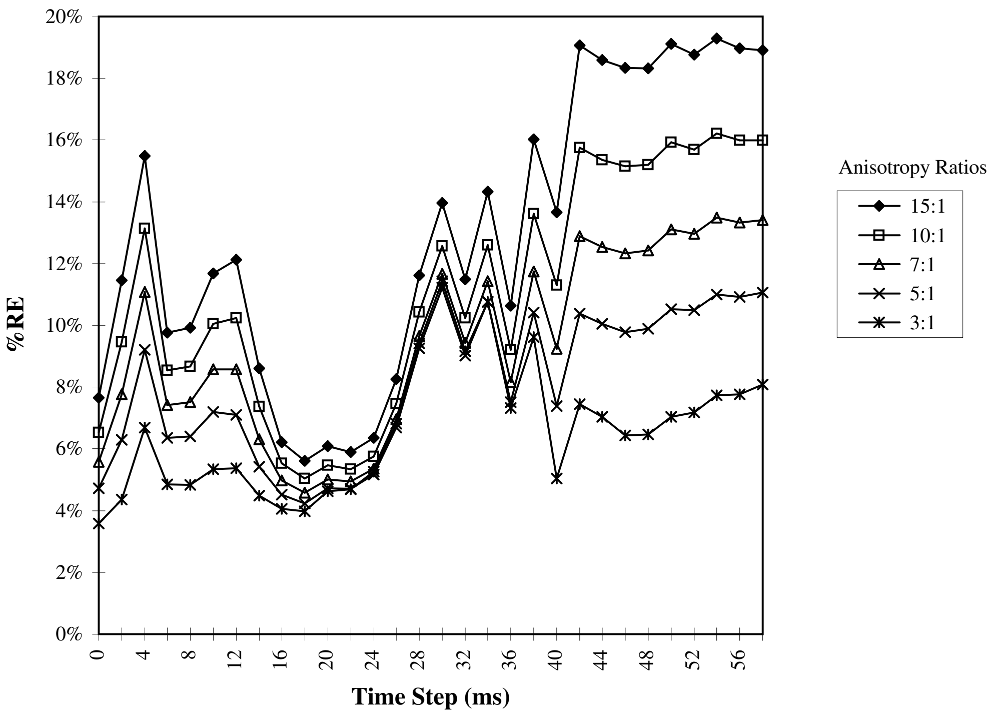

Fig. 8. The RE values comparing BSPMs from the homogenous torso to those generated using a range of muscle anisotropy values in the torso model. Note the change in vertical axis scaling compared to previous plots.

The RE values for the fully detailed model are also included in both for comparison. The changes produced by including two of the inhomogeneities—the isotropic skeletal muscle and bone—were too small to include in the figures.

Figures 6 and 7 include examples of a finding seen throughout the studies; the relative error induced by many inhomgeneities depended strongly on the time instant, and, hence, on the potential distribution at each time instant. For example, the RE values for the right lung were among the smallest in both figures for the early part of the beat, but then increased to the first or second largest amplitude by the latter 15 ms of the QRS.

Another finding from Figures 6 and 7 is that the inhomogeneities of the more anisotropic skeletal muscle and the lungs generally had more influence on model error than the other inhomogeneities. This was most consistently the case late in the QRS. During early QRS, the error values for lungs tended to be smaller than, for example, those from the subcutaneous fat or skeletal muscle at lower anisotropy ratios.

Five different skeletal muscle anisotropy ratios were tested. Figure 8 shows the RE values for the different ratios. The notable finding here is that the level of error produced increased monotonically with the degree of anisotropy.

Figure 9 shows a compressed version of the information in Figures 6 and 7 – the average RE computed across all time instances between the homogeneous torso and those with the single inhomogeneities listed. They are ordered according to size of effect and thus represent a mean ranking of the effects of different inhomogeneities.

Figure 10 and 11 show the CC values for the same simulations from which Figures 6, 7, and 9 were derived. Just as for the relative error results, data for isotropic skeletal muscle and for bones were not included and the curves were split into two plots to improve readability. A comparison of RE and CC results reveals that the changes that occured by adding single inhomogeneities were more evident in

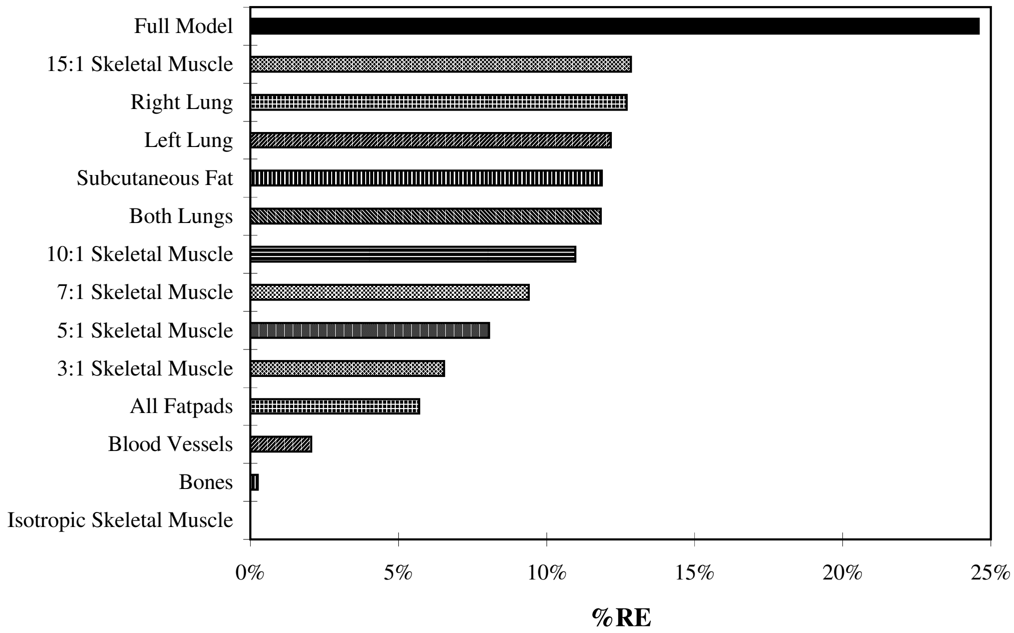

Fig. 9. Average RE values across all time steps between the BSPMs for the inhomogeneity listed and those from the homogeneous case.

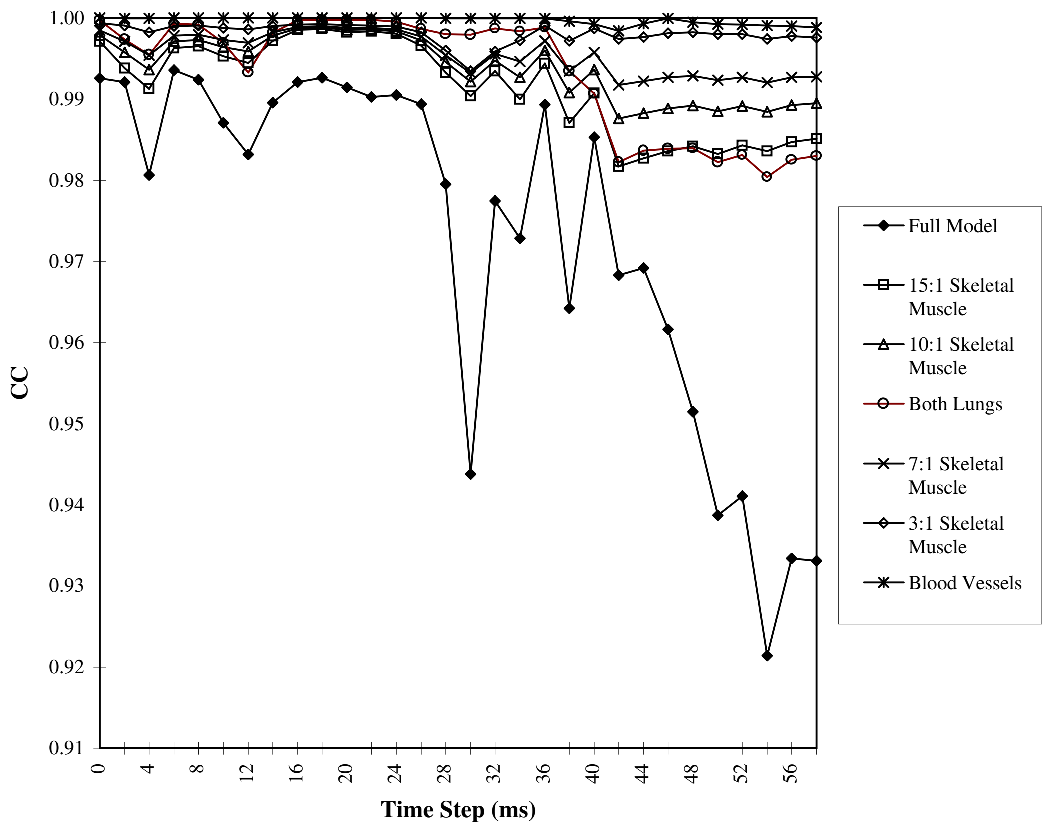

Fig. 10. The correlation coefficients between BSPMs of the homogeneous torso and the those from the torso with the listed additional inhomogeneity as a function of time.

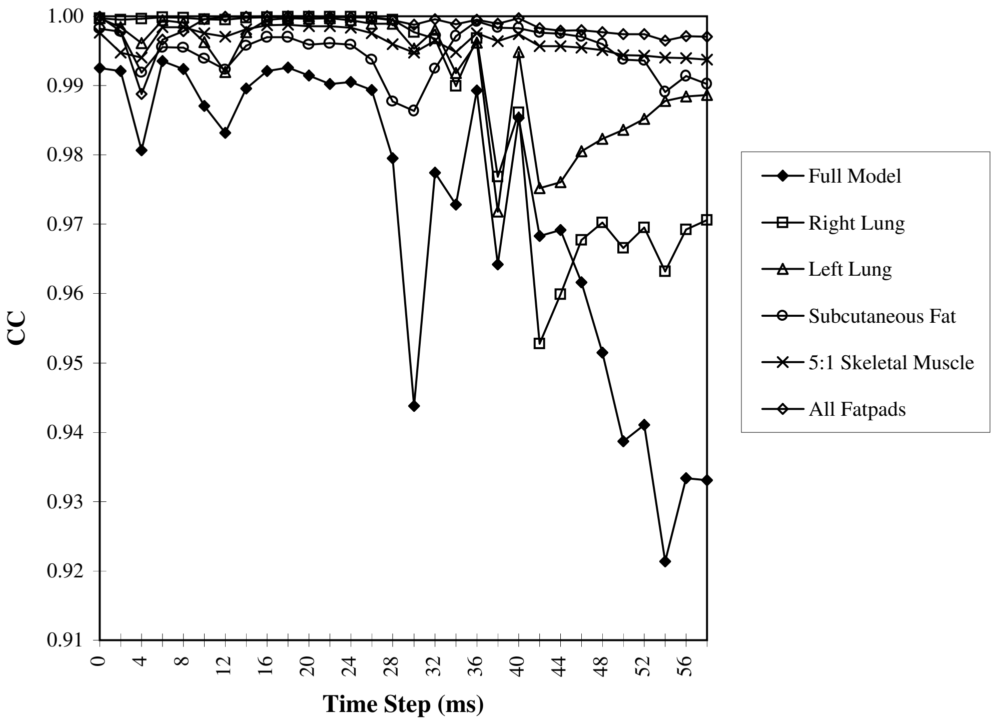

Fig. 11. The correlation coefficients between BSPMs of the homogeneous torso and the those from the torso with the listed additional inhomogeneity as a function of time.

the relative error than in the correlation coefficient.

Figure 12 summarizes Figures 10 and 11 into a single value for each inhomogeneity—the average CC across all time instances. The inhomogeneities are listed in descending order of their effects and we see that the ranking is almost the same as that in Figure 9. The two exceptions are that the right lung is switched with the 15:1 skeletal muscle and the subcutaneous fat dropped below the 10:1 skeletal muscle for the correlation coefficient data. Again, the findings of the RE data are reiterated here: the anisotropic skeletal muscle with larger longitudinal-to-radial fiber ratios and the lungs showed the larger effects.

Figure 13 shows qualitatively the effects of including 15:1 skeletal muscle on the BSPMs of the model. The top row of the figure shows BSPMs generated from the homogeneous model; the BSPMs in the middle row were computed with 15:1 skeletal muscle included in the model. The bottom row shows the difference maps generated by subtracting the skeletal muscle map from the homogeneous map. The number in the upper left corner of each map is the time instant the map represents. The influence of the anisotropic skeletal muscle can be seen in the tendency for the isocontours of the skeletal muscle maps to be slightly more horizontal than the corresponding homogeneous model maps, a possible effect of the circumferential implementation of the skeletal muscle anisotropy.

The second set of simulations considered the difference between BSPMs of the full inhomogeneous model and the same model with one inhomogeneity removed. Figures 14 and 15 show the RE values calculated at each time instant for each of the inhomogeneities listed. The data for the homogeneous model is included in both figures for reference. The symmetry of the two types of simulations performed dictates that the difference between the homogeneous model and that with all inhomogeneities include, as shown in the first set of results, must be identical to the difference between the fully inhomogeneous model and that with all inhomogeneities removed, as shown in the second set of simulations. While comparison of, for example, Figures 6 and 14 suggests otherwise, the discrepancy lies only in the

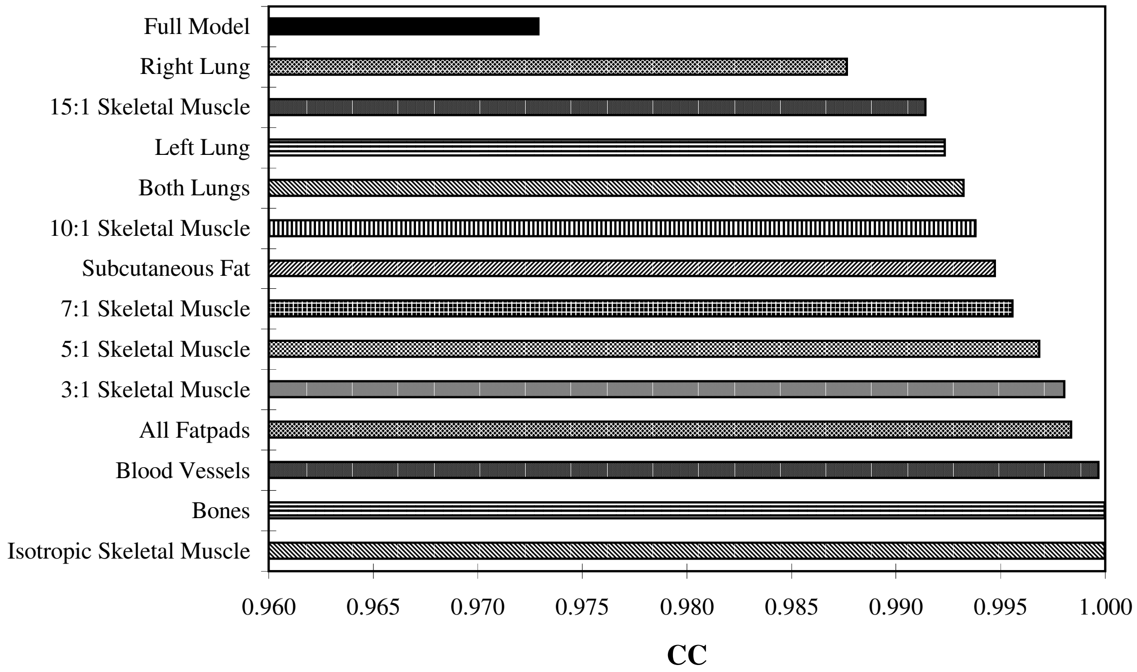

Fig. 12. Average correlation coefficient across all time steps between the BSPMs for the inhomogeneity listed and those computed from the homogeneous case.

nature of the relative error calculation in which a different reference dataset was chosen based on the perspective. The correlation coefficient results presented below do not suffer from this bias and demonstrate identical results in both comparisons.

Figure 16 shows the average RE computed across all time instances between the fully inhomogeneous model and the full model with the inhomogeneity listed removed.

Figures 17 and 18 show the CC calculated for each inhomogeneity at each time step and Figure 19 shows the averages for each inhomogeneity across all time steps. Figure 20 demonstrates the differences between BSPMs in the second set of simulations qualitatively. The top row shows BSPMs of the full model; the middle row shows the maps of the full model without subcutaneous fat. The bottom row shows the difference between these two maps at each time instant.

V. Discussion

Both the RE and the CC comparisons of the first set of simulations demonstrate the effects of adding inhomogeneities to the model. Note that in all cases, the average error did not get within 10% of the error between homogeneous and fully inhomogeneous models, suggesting that no single inhomogeneity can serve as surrogate for the complexity of the full model. Furthermore, only at anisotropy ratios at or above 10:1 did skeletal muscle play a significant role compared to the lungs and the subcutaneous fat. A further finding of note was that while fat located near the torso surface had a strong effect, fat with the same conductivity located on the epicardial surface exerted relatively minor influence. We note, however, that the fat pads used for this study covered only a portion of the epicardium and were quite small (from approximately 20×15 mm to 45×30 mm) compared to the sizes of the fat pad(s) seen in some patients. One would expect that as the size of a fat pad increased, it would play a more significant role in the overall rankings. Curious also was the finding that the inclusion of each lung

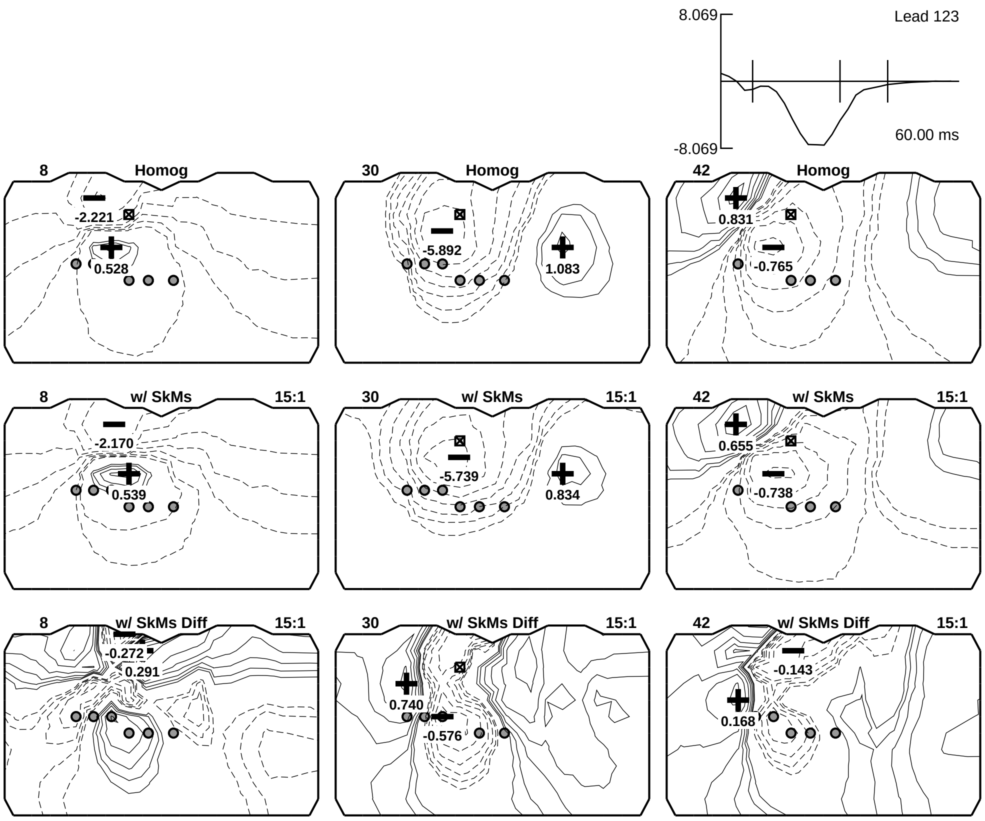

Fig. 13. Computed BSPMs under different conductivity assumptions. Layout of the maps is identical to that in Figure 5. The rows of maps differ in the conductivities assumed with the homogenous torso used to generate the results shown in the uppermost row, the 15:1 skeletal muscle added to the homogeneous model in the middle row and their difference displayed in the lowest row.

individually resulted in slightly larger deviation from the homogeneous model than the combination of both lungs. Hence, a simple additive relationship among the inhomogeneities would seem unlikely. This finding is further supported by the result that adding some individual inhomogeneities resulted in larger deviations from the homogeneous torso than the full model, at least for a few instants over the course of the QRS. For example, in Figure 6 we see that the right lung had greater RE values for several time instants than the fully inhomogeneous case and in Figure 7 the left lung had the largest RE at one time instant.

While the results of selective removal of inhomogeneities reinforced some findings observed when individual inhomogeneities were added, they also revealed important differences. Common to both sets of results was that the effects of an inhomogeneity depended on the field distribution and hence changed sharply from instant to instant during the QRS. Likewise, the inhomogeneities that were located near the bottom of the average error plots—and thus lowest in order of influence—included the bone and individual fatpads in both sets of studies. Among the contrasts between addition and removal of inhomogeneities were the stronger influences of the *removal* of the 7:1 anisotropic muscle compared to the effects of *adding* it. Figures 9 and 16 reveal that the individual removal resulted in a relative error of about 14% while their addition to a homogeneous model changed the RE by less than 10%. The difference between removal and addition of inhomogeneities is further demonstrated by the result that in no case did the removal of a single inhomogeneity result in error appreciably greater than the homogeneous torso (although subcutaneous fat had slightly greater error in two time instants). The time course of the effect of an inhomogeneity also differed between addition and removal of single inhomogeneities. For example, addition of the great blood vessels played only a small role throughout

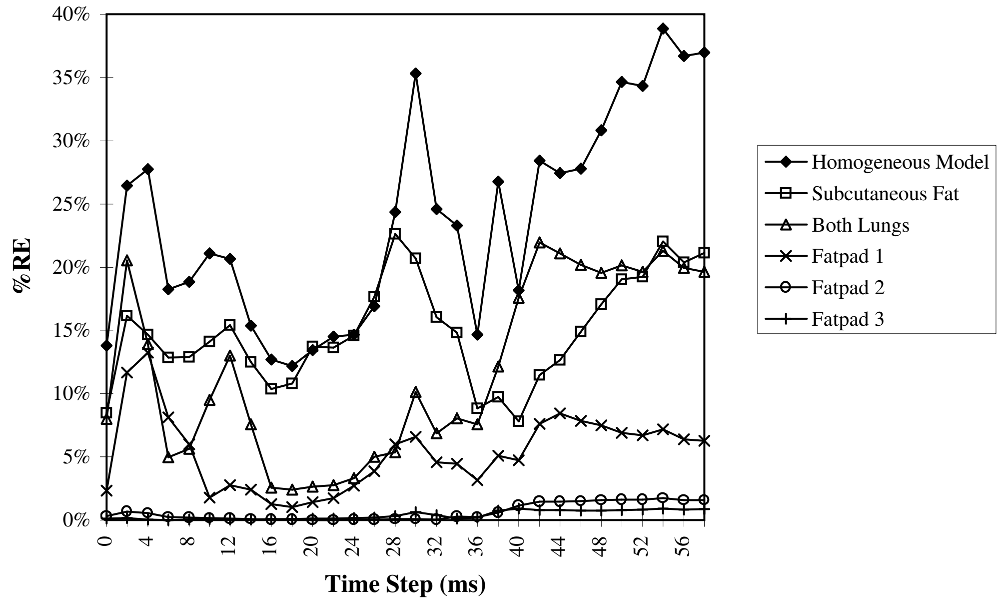

Fig. 14. Values of RE between BSPMs computed using the full inhomogeneous model compared to those computed when each of the listed inhomgeneous regions was "removed", *i.e.,* given the same conductivity value as the homogeneous torso model.

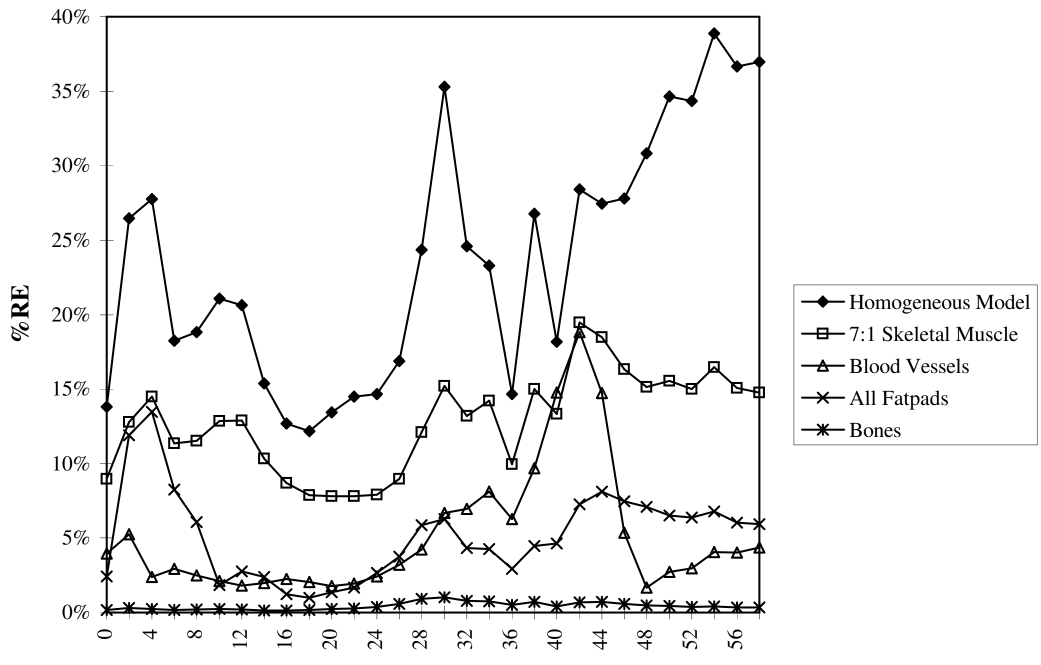

Fig. 15. Values of RE between BSPMs computed using the full inhomogeneous model compared to those computed when each of the listed inhomgeneous regions was "removed".

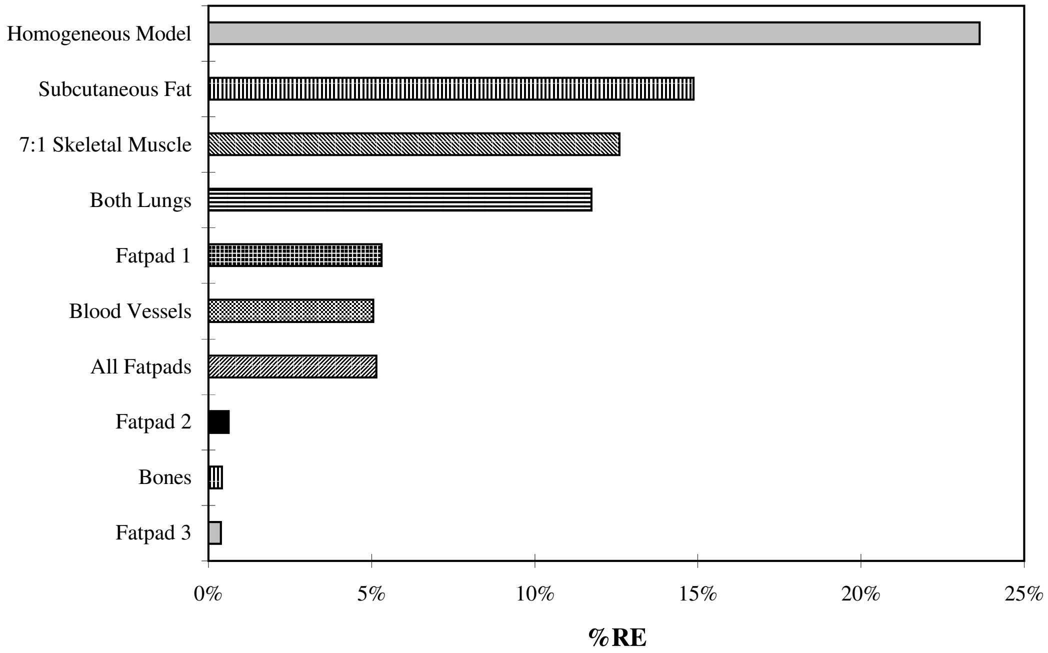

Fig. 16. Average RE values across all time steps between BSPMs of the full model and the those using the full model with the listed inhomogeneity removed.

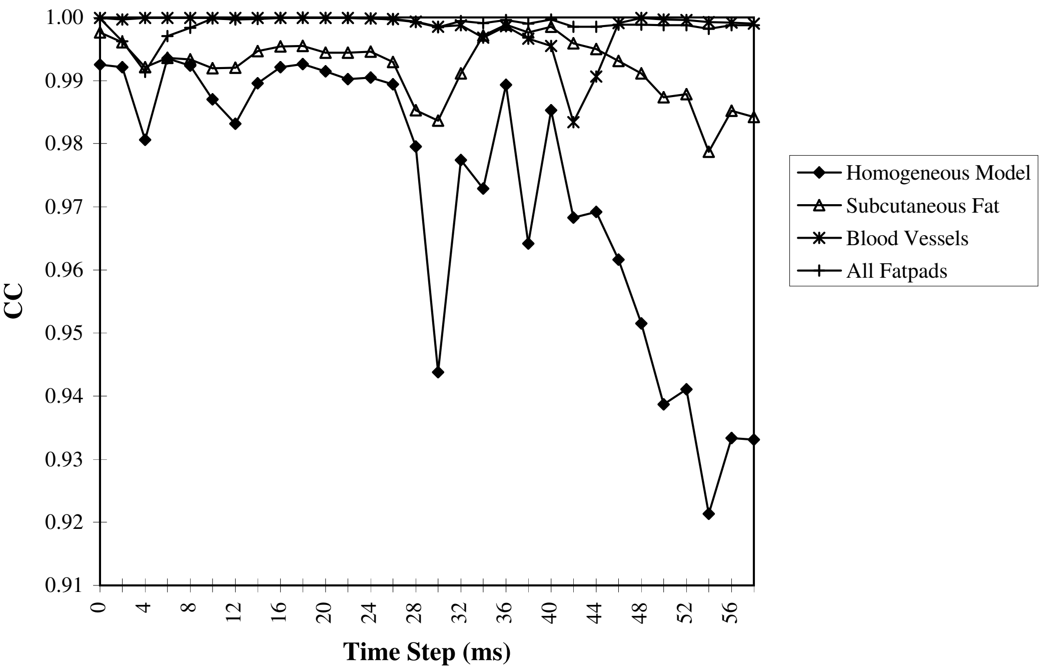

Fig. 17. The correlation coefficients as a function of time between BSPMs of the full model and those of the model with the single inhomogeneity listed removed.

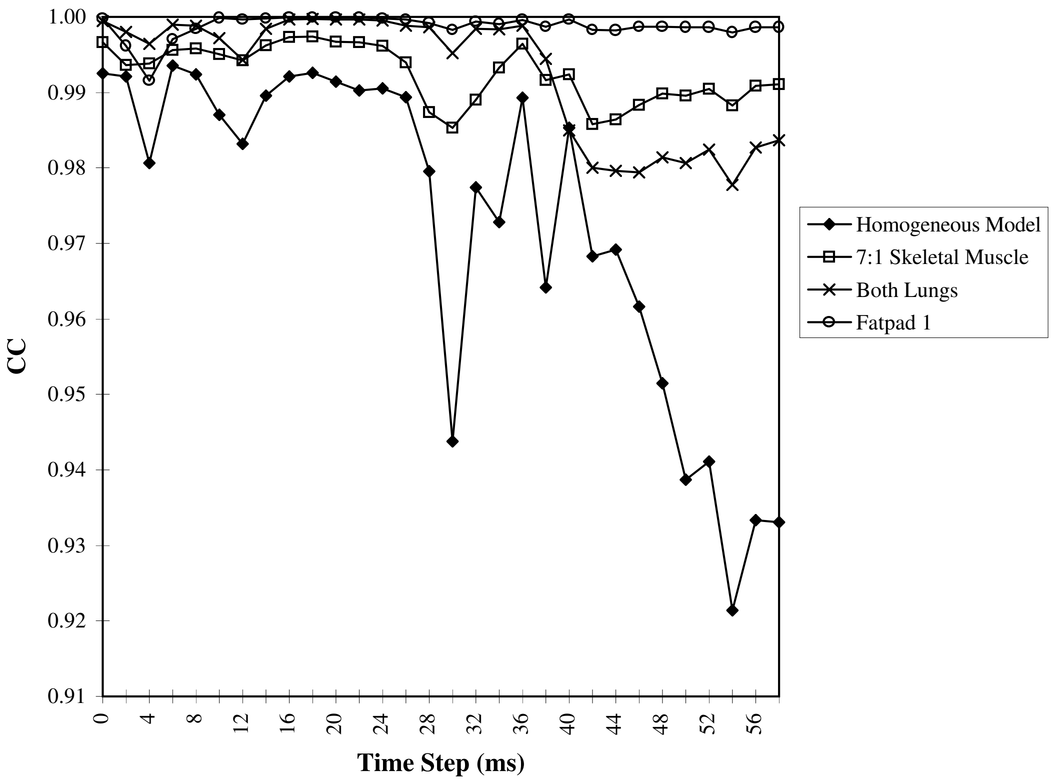

Fig. 18. The correlation coefficients as a function of time between BSPMs of the full model and those of the model with the single inhomogeneity listed removed.

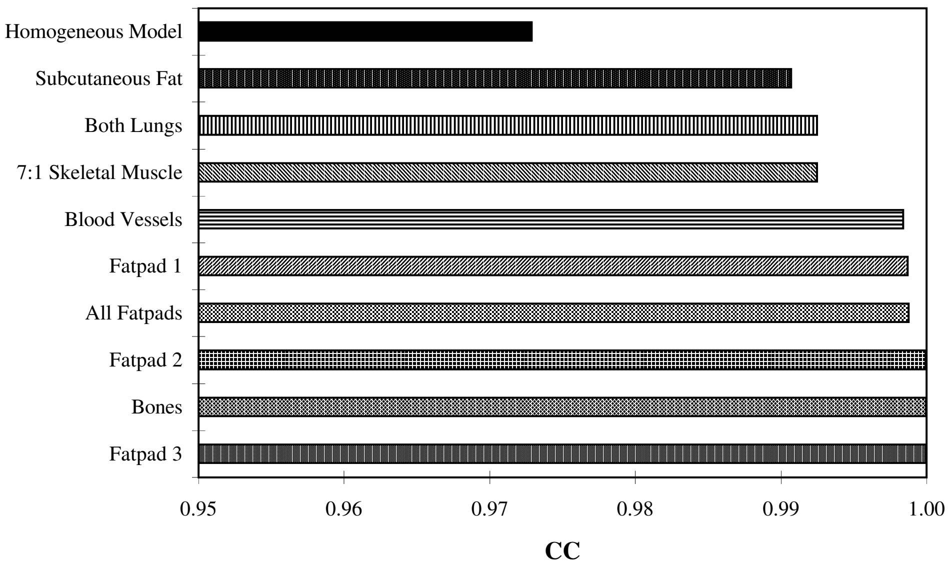

Fig. 19. Average correlation coefficient across all time steps between BSPMs of the full model and those from the model with the listed inhomogeneity removed.

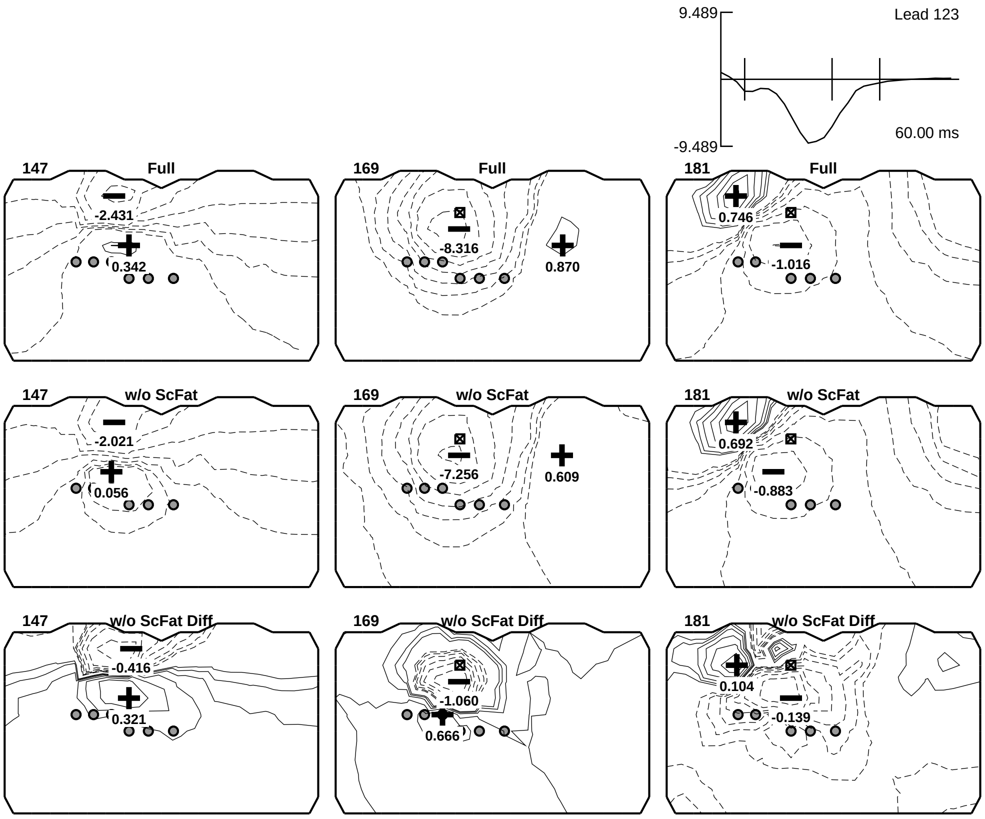

Fig. 20. Computed BSPMs under different conductivity assumptions. Layout of the maps is identical to that in Figure 5. The rows of maps differ in the conductivities assumed with the full inhomogenous torso used to generate the results shown in the uppermost row, the full torso without subcutaneous fat in the middle row and their difference displayed in the lowest row.

the QRS, as shown in Figure 6; removal of the same inhomgeneity, on the other hand, resulted in fluctuating relative errors ranging from 2% to almost 20% over the course of the beat, as shown in Figure 15.

The shape of the histograms in Figures 9 and 16 also reveal differences between addition and removal of single inhomogeneities from the model. While the distribution in Figure 9 is relatively smooth for the addition of each individual inhomogeneity, the distribution in Figure 16 can be divided into three bands with clear differences in relative error between each band. From this, one can see that removal of subcutaneous fat, skeletal muscle (at anisotropy 7:1), and the lungs had the largest impact, with all the fatpads, fatpad 1 and the blood vessels at less than half the relative error and the other fatpads and bone having almost no influence on the accuracy of the forward solutions. A similar banding pattern is also seen in Figure 19.

The plots of the BSPMs from specific instants in time serve to provide some sense of the spatial differences that arose when the model conductivity was varied. In all the cases shown in Figures 13 and 20, the effects of addition or removal of even the single most important inhomogeneity did not change the coarse features of the maps; the maxima and minima remained in approximately the same locations and the overal topography of the maps was stable. The nature of the changes observed was in the shape of the features and in their amplitudes, with peaks and valleys typically becoming sharper as more complexity was added to the model. The findings have important consequences for the interpretation of our quantitative results and their practical application to forward and inverse problems. In many cases, the level of accuracy offered by even a homogeneous model may be adequate to reveal general features of the torso potentials from known epicardial signals. It is perhaps even more important to compare the level of error induced by a lack of fidelity in conductivity, as we have done, to that arising from lack of geometric resolution. A study that incorporates both these sources of error in a systematic manner with realistic torso geometry does not, to our knowledge, exist.

In the context of relevant results from the literature, our results support some aspects of previous studies [30], [11], [31], [12], with significant enhancement due to our ability to model anisotropy directly. A fundamental difference of this study from all others to our knowledge is that we computed the forward solution, *i.e.,* the torso potentials from known epicardial potentials, not the inverse solution. Early studies by Messinger-Rapport and Rudy using an eccentric spheres model [30] suggested that the influence of idealized "lungs" and isotropic "muscle" layers was exclusively a change in amplitude of computed surface potentials with no shift in the topography of the distribution. While the simplicity of the geometry in this study permitted analytic solutions to the forward and inverse problem, it suffered from unrealistic symmetry and complete containment of the heart by the single, concentric lung layer. Stanley *et al.* conducted studies based on digitized models of an animal in which epicardial and torso surface potentials had been measured simultaneously [11] and found that skeletal muscle had the largest role in the accuracy of computed inverse solutions. Their numerical method, however, did not permit direct inclusion of anisotropy so they used a method suggested by McFee and Rush in which the isotropic muscle layer is artificially expanded radially by an amount related to the degree of anisotropy [32]. Their model also lacked subcutaneous fat, but did suggest that inhomogeneities close to the outer surface played the largest role in model accuracy, in general agreement with our results.

Among studies based on human data, reports by Walker and Kilpatrick [31] and Purcell *et al.* [33] noted the dominant influence of the lungs in inverse solution accuracy, as well as the relatively minor contribution of bone, again in qualitative agreement with our results. On the other hand, studies by Van Oosterom and Huiskamp on an inverse model based on the epicardial and endocardial activation sequence [12] suggest that removal of the lungs added perhaps a few percent to the relative error of their inverse solution. Much more critical were the blood filled chambers of the ventricles, which are unique to their model formulation and hence play no role in our simulations.

While our results suggest that accurate descriptions of tissue conductivity improves the quality of the simulations, this is not the only component of a complete forward solution. The level of discretization in the geometric model clearly plays a role in simulations and we have used 168,000 nodes and nearly one million elements for the results presented here. To evaluate, at least coarsely, the effects of node spacing, we created a second homogeneous model based on the same geometry as the original model but with only 62,000 nodes and then repeated the simulation of BSPMs. The results differed only slightly from those using the more finely meshed model (mean CC=.9991 and mean RE=4.8%). Although only a complete study of the effects of geometry on model results would confirm these results generally, the larger differences found due to conductivity changes suggests that our results are reasonably independent of model geometry.

None of the studies of inhomogeneities known to us have included the level of detail in the geometrical model or the range of accurately modeled tissues we have employed. Hence, while general concurrance of a few of our findings with previous investigations is encouraging, we feel our findings contain unique contributions to the modeling of bioelectric fields in realistic conditions.

VI. Conclusion

This study provides quantitative data on the effects of including or excluding selected inhomogeneities and anisotropies when solving the forward ECG problem within a realistic finite element model of the human thorax.

The influence of these findings on the design of torso models for forward computations can be summarized in the following points:

1. Models consisting of a single inhomogeneous region will always incur significant errors compared to those that incorporate a more complete representation of torso inhomogeneity. No realistic

single-inhomogeneity model was capable of getting within 10% (RE) of the fully inhomogeneous model.

2. The effects demonstrated by either adding or removing inhomogeneities appeared to have only minor influence on the location of features of the BSPM but instead altered the shape and magnitude of these features.
3. In a multi-component model, removal of subcutaneous fat, the anisotropic skeletal muscle, or the lungs from an otherwise "complete" model will result in errors comparable to the best of the single-inhomogeneity models. Hence, these components must be considered crucial to such a model of the thorax.
4. The influence of skeletal muscle depends strongly and monotonically on the degree of anisotropy incorporated.
5. The influence of different inhomogeneities depends on the potential field distribution in ways that are not easily predictable, both in terms of absolute errors and the relative errors induced by addition or removal of individual inhomogeneities.

The information provided in these results demonstrates the effects of various structures that may be included in finite element models of electrocardiographic fields. The actual value at which an effect becomes important is dependent on the particular modeling application. Details that change the results by a small amount may not be worth including for some modeling applications, while this same detail may be critical in a different application, such as solving the electrocardiographic inverse problem. The results of this study will allow researchers to make quantitative comparisons of different modeling options and help them better optimize the use of their computational resources.

VII. Acknowledgements

This research was supported in part by awards from the NIH, NSF, Whitaker Foundation, and Medtronic Corporation. The authors would like to thank K. Coles, Y. Livnat, J. Schmidt, and D. Weinstein for their helpful comments and suggestions.

References

[1] C.R. Johnson, R.S. MacLeod, and M.A. Matheson. Computer simultions reveal complexity of electrical activity in the human thorax. *Comp. in Physics*, 6(3):230–237, May/June 1992.

[2] C.E. Miller and C.S. Henriquez. Finite element analysis of bioelectric phenomena. *Crit. Rev. in Biomed. Eng.*, 18:181–205, 1990.

[3] P. Colli Franzone, B. Taccardi, and C. Viganotti. An approach to inverse calculation of epicardial potentials from body surface maps. *Adv. Cardiol.*, 21:50–54, 1978.

[4] D.G. Gisser, D. Isaacson, and J.C. Newll. Electric current computed tomography and eigenvalues. *SIAM J. Appl. Math.*, 50:1623–1634, 1990.

[5] Y. Rudy and H. Oster. The electrocardiographic inverse problem. *CRC Crit. Rev. Biomed. Eng.*, 20:22–45, 1992.

[6] C.R. Johnson, R.S. MacLeod, and M.A. Matheson. Computational medicine: Bioelectric field problems. *IEEE Computer*, 26(10):59–67, Oct. 1993.

[7] J.A. Schmidt, C.R. Johnson, and R.S. MacLeod. An interactive computer model for defibrillation device design. In T. Oostendorp and G. Oiju, editors, *Building Bridges: International Congress on Electrocardiology International Meeting*, pages 160–161, 1995.

[8] Bayley R.H. and Berry P.M. The electrical field produced by the eccentric current dipole in the nonhomogeneous conductor. *Am. Heart J.*, 63, 1962.

[9] R.H. Bayley, J.M. Kalbfleisch, and P.M. Berry. Changes in the body's QRS surface potentials produced by alterations in certain compartments of the nonhomogeneous conducting model. *Am. Heart J.*, 77, 1969.

[10] Y. Rudy and R. Plonsey. The effects of variations in conductivity and geometrical parameters on the electrocardiogram, using an eccentric spheres model. *Circ. Res.*, 44(1):104–111, 1979.

[11] P.C. Stanley, T.C. Pilkington, and M.N. Morrow. The effects of thoracic inhomogeneities on the relationship between epicardial and torso potentials. *IEEE Trans Biomed. Eng.*, BME-33:273–284, 1986.

[12] A. van Oosterom and G.J. Huiskamp. The effect of torso inhomogeneities on body surface potentials quantified using "tailored" geometry. *J. Electrocardiol.*, 22:53–72, 1989.

[13] C.R. Johnson and R.S. MacLeod. A computer model for calculating electric and potential fields in the human thorax. *Ann. Biomed. Eng.*, 19:620, 1991. Proceedings of the 1991 Annual Fall Meeting of the Biomedical Engineering Society.

[14] C.R. Johnson, R.S. MacLeod, and A. Dutson. Effects of anistropy and inhomogeneity on electrocardiographic fields: a finite element study. In *IEEE Engineering in Medicine and Biology Society 14th Annual International Conference*, pages 2009–2010. IEEE Press, 1992.

[15] R.S. MacLeod, C.R. Johnson, and P.R. Ershler. Construction of an inhomogeneous model of the human torso for use in computational electrocardiography. In *IEEE Engineering in Medicine and Biology Society 13th Annual International Conference*, pages 688–689. IEEE Press, 1991.

[16] K.R. Foster and H.P. Schwan. Dielectric properties of tissues and biological materials: a critical review. *Crit. Rev. in Biomed. Eng.*, 17:25–104, 1989.

[17] R. Plonsey. *Bioelectric Phenomena*. McGraw-Hill, New York, 1969.

[18] J.D. Jackson. *Classical Electrodynamics*. John Wiley, New York, 1975.

[19] John G. Webster. *Medical Instrumentation: Application and Design*. Houghton Mifflin, Boston, 1978.

[20] R. Plonsey. Introductory physics and mathematics. In P.W. Macfarlane and T.D. Veitch Lawrie, editors, *Comprehensive Electrocardiology*, chapter 2, pages 41–76. Pergamon Press, Oxford, England, 1989. Volume 1.

[21] C.R. Johnson, R.S. MacLeod, and P.R. Ershler. A computer model for the study of electrical current flow in the human thorax. *Computers in Biology and Medicine*, 22(5):305–323, 1992.

[22] P.R. Ershler, R.L. Lux, L.S. Green, G.R. Caputo, and D. Parker. Determination of 3-Dimensional torso, heart, and electrode geometries from magnetic resonance images. In *IEEE Engineering in Medicine and Biology Society 10th Annual International Conference*, pages 121–122. IEEE, 1988.

[23] H.W. Shen and C.R. Johnson. Semi-automatic image segmentation: A bimodel thresholding approach. Technical report, UUCS-94-019, Dept. of CS, Univ. of Utah, 1994.

[24] J. Schmidt. *Mesh generation with applications in computational electrophysiology*. PhD thesis, Duke University, Durham, NC, 1993.

[25] J.A. Schmidt, C.R. Johnson, J.A. Eason, and R.S. MacLeod. Applications of automatic mesh generation and adaptive methods in computational medicine. In J. Flaherty and I. Babuska, editors, *Modeling, Mesh Generation, and Adaptive Methods for Partial Differential Equations*, pages 367–394. Springer Verlag, 1994.

[26] L. DeAmbroggi, B. Taccardi, and E. Macchi. Body surface maps of heart potential: Tentative localization of preexcited area of forty-two Wolff-Parkinson-White patients. *Circ.*, 54:251, 1976.

[27] P.R. Lux and P.R. Ershler. Reducing uncertainty in the measures of cardiac activation and recovery. In *IEEE Engineering in Medicine and Biology Society 9th Annual International Conference*, pages 1871–1872. IEEE Press, 1987.

[28] T.F. Oostendorp, A. van Oosterom, and G.J. Huiskamp. Interpolation on a triangulated 3D surface. *J. Comp. Physics*, 80:331–343, 1989.

[29] R.S. MacLeod, R.L. Lux, and B. Taccardi. Translation of body surface maps between different electrode configurations using a three-dimensional interpolation scheme. In P.W. MacFarlane, editor, *Electrocardiology '93: Proceedings of the International Congress on Electrocardiology, XXth Annual Meeting*, pages 179–182. World Scientific, Singapore, 1993.

[30] B.J. Messinger-Rapport and Y. Rudy. The inverse problem in electrocardiography: A model study of the effects of geometry and conductivity parameters on the reconstruction of epicardial potentials. *IEEE Trans Biomed. Eng.*, BME-33:667–676, 1986.

[31] S.J. Walker and D. Kilpatrick. Forward and inverse electrocardiographic calculations using resistor network models of the human torso. *Circ. Res.*, 61:504–513, 1987.

[32] R. McFee and S. Rush. Qualitative effects of thoracic resistivity variations on the interpretation of the electrocardiograms: the low resistance surface layer. *Am. Heart J.*, 76:48–61, 1968.

[33] C.J. Purcell, G. Stroink, and B.M. Horáček. Effect of torso boundaries on electrical potential and magnetic field of a dipole. *IEEE Trans Biomed. Eng.*, BME-35:671–678, Sep 1988.

Ruth Nicholson Klepfer received her B.S.E. in Biomedical Engineering from the University of Iowa in 1989. She is currently a Ph.D. student in Bioengineering at the University of Utah working on her degree remotely from Minneapolis, Minnesota. She was a University of Utah Presidential Fellow in 1992. Her research interests include modeling and simulation in medicine and physiology, particularly large-scale problems in electrophysiology.

Christopher Johnson received his Ph.D. from the University of Utah in 1989. He is an Associate Professor in the Department of Computer Science at the University of Utah. His research interests are in the area of scientific computing. Particular interests include inverse and imaging problems, adaptive methods for partial differential equations, numerical analysis, computational problems in medicine, and scientific visualization. In 1992, Professor Johnson was awarded a FIRST Award from the NIH, a National Young Investigator (NYI) Award from the NSF in 1994, and the Presidential Faculty Fellow (PFF) Award in 1995. He directs the Center for Scientific Computing and Imaging (SCI) at the University of Utah.

Robert S. MacLeod received both his B.Sc. ('74) in Engineering Physics and his Ph.D. ('90) in Physiology and Biophysics from Dalhousie University. His M.Sc. ('85) in Electrical Engineering came from the Technische Universität, Graz, Austria. He is an Assistant Professor in the Department of Internal Medicine (Div. of Cardiology) and Dept. of Bioengineering at the University of Utah, and a member of the Nora Eccles Harrison Cardiovascular Research and Training Institute. His research interests include computational electrocardiography (forward and inverse problems), experimental investigation and clinical detection of cardiac ischemia and repolarization abnormalities, and scientific computing and visualization.